

Design of a multi-axis implantable MEMS sensor for intraosseous bone stress monitoring

Fernando Alfaro¹, Lee Weiss², Phil Campbell², Mark Miller^{3,4} and Gary K Fedder²

¹ Silicon Microstructures, Inc., Milpitas, CA 95035, USA

² Carnegie Mellon University, Pittsburgh, PA 15213, USA

³ Allegheny General Hospital, Pittsburgh, PA 15224, USA

⁴ University of Pittsburgh, Pittsburgh, PA 15260, USA

Received 12 February 2009, in final form 22 April 2009

Published 14 July 2009

Online at stacks.iop.org/JMM/19/085016

Abstract

The capability to assess the biomechanical properties of living bone is important for basic research as well as the clinical management of skeletal trauma and disease. Even though radiodensitometric imaging is commonly used to infer bone quality, bone strength does not necessarily correlate well with these non-invasive measurements. This paper reports on the design, fabrication and initial testing of an implantable ultra-miniature multi-axis sensor for directly measuring bone stresses at a micro-scale. The device, which is fabricated with CMOS-MEMS processes, is intended to be permanently implanted within open fractures, or embedded in bone grafts, or placed on implants at the interfaces between bone and prosthetics. The stress sensor comprises an array of piezoresistive pixels to detect a stress tensor at the interfacial area between the MEMS chip and bone, with a resolution to 100 Pa, in 1 s averaging. The sensor system design and manufacture is also compatible with the integration of wireless RF telemetry, for power and data retrieval, all within a 3 mm × 3 mm × 0.3 mm footprint. The piezoresistive elements are integrated within a textured surface to enhance sensor integration with bone. Finite element analysis led to a sensor design for normal and shear stress detection. A wired sensor was fabricated in the Jazz 0.35 μm BiCMOS process and then embedded in mock bone material to characterize its response to tensile and bending loads up to 250 kPa.

(Some figures in this article are in colour only in the electronic version)

1. Introduction

Non-invasive assessment of the biomechanical properties of living bone primarily relies on measurements of the bone mineral density to infer mechanical strength. Radiodensitometric techniques are the most predominant methods used clinically. Dual energy x-ray absorptometry, which is a two-dimensional imaging approach, is the current worldwide standard, while quantitative computed tomography is a more exacting approach but requiring substantially higher radiation doses [1, 2]. Alternatively, ultrasound can be used to estimate bone density and some structural information derived from alterations in velocity and attenuation of ultrasound

waves passing through bone [1–4]. This approach does not impart radiation, therefore can be safer to use. The use of low-frequency vibration to measure bone mechanical properties, although investigated extensively since the 1930s, has been surpassed by ultrasound due to the interference of soft tissues surrounding bone with vibrational analysis and the heterogeneous nature of bone itself [5]. Basically, all of these techniques indirectly infer bone mechanical properties and do not necessarily correlate well with bone strength. Accurate and reliable assessment of strength requires direct measurements. Such direct biomechanical measurements of bone *in vivo* use surgically implanted strain gages mounted on internal fixators [6–9], prosthetics [10] or bone surfaces [11–13]. However,

these types of sensors have been used primarily for research; their cost and added surgical requirements have thus far made them impractical for use in routine clinical application where they could potentially provide timely feedback for post-surgical management.

Benzel *et al* [14] describe a microminiature MEMS pressure sensor, interfaced to a separate RF coil for power and telemetry, which would be embedded directly within bone grafts to provide even more direct and sensitive information on bone healing in applications such as spinal fusion monitoring. We believe that there is a need for similar embedded intraosseous sensors which, in addition, could provide multi-axis stress information and also integrate sensing and RF telemetry in a single microminiature chip that would be easy to deploy. Multi-axial sensing is important because of the anisotropic characteristics of bone; although bone has some structural symmetry, material properties will typically vary in all three orthogonal directions [15]. Microminiature sensors could be easily placed in open fractures at the time of surgical repair. Such sensors could also be deployed on implants to provide information about bone–implant interfaces at a micro-scale, including capturing the effects of crack, friction or implant de-cohesion. Implant loosening, for example, is a severe problem leading to revision surgery [16]. Detection of those cases requiring surgery would benefit patients and reduce costs.

RF on-chip inductor-capacitor resonators have been proposed as implantable strain sensors by measuring the resonator frequency shift with mechanical deformation of the chip and experimentally measured at very high loads over 1900 N for potential use with steel plate implants [17]. The present work focuses on sensor development for bone healing applications where the physician applies relatively small loads on the order of 1–10 N. The sensor proposed in [17] couples two coils on the same substrate in sub-mm proximity using a drive from external RF probes; it does not address the problem of wireless power or operation through centimeters of tissue. Furthermore, this passive resonator approach does not address multi-axis sensing nor does the chip implementation address osteointegration issues. Multi-axis stress sensing is necessary to objectively evaluate healing of bone given its anisotropy and complex micro-structure.

We previously proposed a wireless microminiature intraosseous sensor system to measure multi-axis stresses at the microscale [18]. The conceptual design of the sensor, depicted in figure 1, includes a central MEMS transducer array, a surrounding coil antenna for wireless operation, and electronics, all integrated on a single 3 mm × 3 mm CMOS chip. The transducer array, which has a 1 mm × 1 mm footprint, is an 8 × 8 array of piezoresistive strain gages that produce the raw data needed to extract a stress tensor.

Wireless operation of the device is outside the scope of this paper, however, it is necessary to discuss some practical issues. This work proposes a radio frequency (RF) system, based on inductive coupling, to transfer power to and communicate wirelessly with the stress sensor. The envisioned electronics include an analog RF interface, tuning capacitor, RF-to-dc rectifier system, digital control and data modulation circuits.

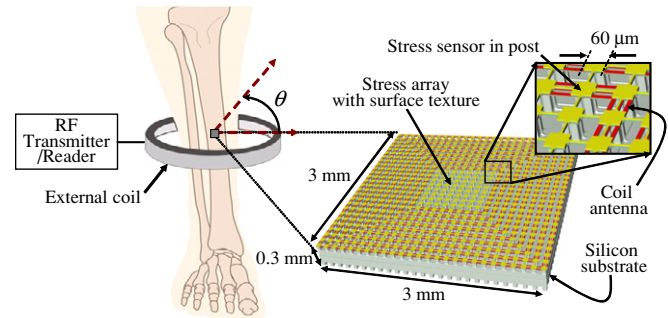


Figure 1. Envisioned implantable CMOS-MEMS multi-axis stress sensor.

The system would communicate with and be powered by an external reader/transmitter using magnetic near-field coupling through a resonant tuned circuit. The resonant frequency is 13.56 MHz. While a much lower frequency can provide less signal attenuation (due to body fluid) over distance, the transponder coil has to be physically larger. On the other hand, a much higher frequency than 13.56 MHz enables use of a smaller receiving coil but suffers from more signal attenuation through tissue. Thus, resonating at 13.56 MHz provides a good compromise for this system. For a 3 mm coil antenna with 27 turns, a 21.8 pF capacitor is required. This is equivalent to capacitor size of 148 μm × 148 μm using a metal–insulator–metal capacitor (1 fF μm⁻²) generally available in RF CMOS technologies. The overall system size will be 3 mm × 3 mm × 0.3 mm, which should have minimum impact on the overall strength of healed bone in which it is embedded. The economies of scale of CMOS-MEMS manufacturing technologies also will keep costs low, and therefore help make these sensors a practical tool for routine clinical application.

In order to measure transmitted or residual loads, it will be important for the transducer to become well integrated with the surrounding bone. The incorporation of surface topography can enhance cell growth and osteointegration [19]. In addition, coating the silicon with titanium further enhances osteoconductivity and biocompatibility [20, 21]. Therefore before proceeding with detailed design of the transducer, we evaluated adult mesenchymal stem cell (hAMSC) and MG-63 cell attachment and differentiation responses *in vitro* to several surface topologies on prototype of silicon chips fabricated with deep reactive ion etching (DRIE) and coated with titanium [18]. Using these studies we determined that arrays of 60 μm square posts that are 60 μm tall and spaced 60 μm apart provided satisfactory results (see figure 2 for an example) [22]. Therefore, the transducer array in figure 1 comprises such posts, and the top of each post incorporates a bridge of four piezoresistive stress-sensing elements and electronics for multiplexer addressing.

After the sensor has been surgically implanted, the system sensor could be used to monitor bone healing in one of two ways. External loads could be applied to the bone during follow-up studies or clinical examinations. We hypothesize that the measured load transmitted into and measured by the sensor will increase as the bone heals around the sensor. We

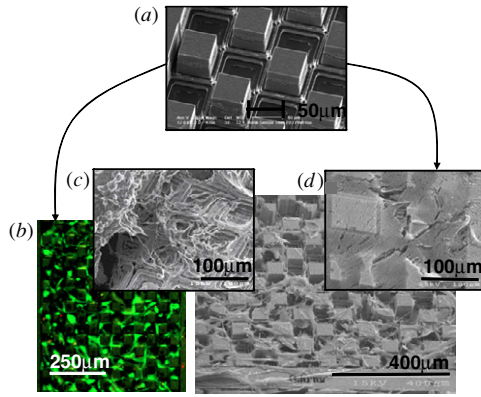


Figure 2. (a) SEM of prototype titanium-coated silicon chip with textured surface composed of 60 μm posts. (b) Live/dead fluorescent staining. Green = alive, red = dead. (c) SEM characterization of with MG-63 cells. (d) Si sensor topography underneath layer of hAMSC [22].

also speculate that measured stresses in the quiescent state (no loads applied) will correlate with bone regeneration due to residual stresses of remodeling.

This paper reports on the next stage of sensor development, including the design, fabrication and testing of the transducer array. A mathematical model is developed to describe the transducer’s characteristics as a function of the orientation of applied stress and verified through finite element analysis. The array is fabricated in the BiCMOS process, and then a wired version is tested by embedding it in mock bone material. The design and fabrication of this transducer is compatible with its integration with an RF coil and electronics on a single chip, as will be described at the end of this paper.

2. Transducer design

2.1. Strain gage design

The analysis for the design of the piezoresistive-based sensor array includes evaluating the sensor’s dynamic range and resolution in relation to multiple design parameters, including resistor doping type (p- or n-), layout geometry, orientation with respect to the crystal silicon and location on the die. Figure 3(a) shows an example of a single silicon post with piezoresistive elements located in the silicon under the oxide layer. The piezoresistors are arranged in a Wheatstone bridge configuration, shown in figure 3(b), and signals are routed with the interconnect stack through the suspended metal/oxide beams. The design goals to be achieved are based on the following assumptions. When the sensor is being used by a physician to evaluate bone healing, we anticipate that the physician will apply an external pressure of around 10 kPa. Then, assuming that a 1% resolution in stress is desired, the required minimum detectable stress for the sensor is 100 Pa. With the additional assumption that a signal-to-noise ratio (SNR) of 10 dB is acceptable, a 32 Pa equivalent input noise is required for each piezoresistive stress sensor in the array. The maximum load that a bone can sustain is in the order of hundreds of kPa at its upper limit. For a conservative design, this application considers a maximum load of 200 kPa.

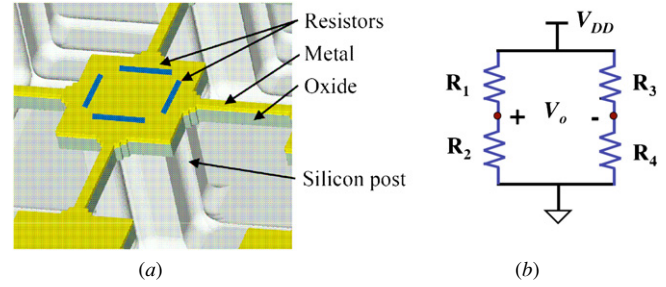


Figure 3. (a) Visualization of a 60 μm by 60 μm by 60 μm tall silicon post indicating the location of piezoresistors in the silicon under the oxide layer. The interconnecting beam consists of metal and oxide layers. (b) Schematic of piezoresistive Wheatstone bridge.

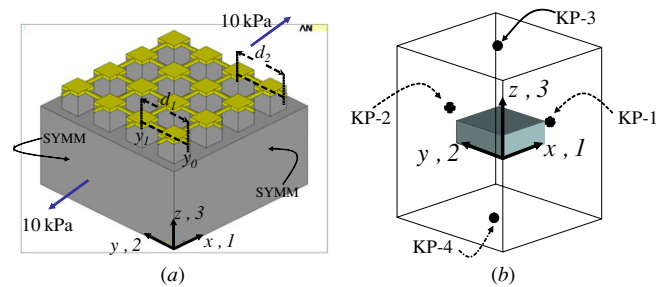


Figure 4. One-quarter symmetric model of a bone stress sensor.

Table 1. Material properties used in FEA.

Material	Young modulus, E (GPa)	Poisson ratio, ν	Density, ρ (kg m ⁻³)
Cortical bone	18	0.39	2000
Silicon	169	0.3	2330
Beam	60	0.17	2200

2.1.1. Finite element analysis. To aid design, finite element analysis (FEA) using ANSYS was used to model a prototype sensor array chip, which is shown in figure 4(a) as a one-quarter symmetric model consisting of a silicon substrate, silicon posts and oxide beams enclosed in a cube of cortical bone (not shown) that extends 1.5 mm around the chip. The simplified prototype did not include the coil from figure 1 and is reduced in size to fit an 8 × 8 array of the 60 μm square posts. The material properties for the FEA solid model are summarized in table 1. To emulate external stimuli, the external faces of the bone are subjected to a set of axial or shear loads along the global axes {x, y, z}. For example, a tensile stress applied to opposite faces of the bone along the x-axis corresponds to stress σ_{xx} . The chip’s local axes {1, 2, 3} are aligned with the {x, y, z} axes. The suspended beams that span between posts are fabricated as part of the CMOS interconnect stack and contain silicon oxide, aluminum/titanium interconnects. The beams are modeled with effective mechanical properties. The silicon mechanics is approximated with a single Young’s modulus.

The FEA simulations guide placement of the piezoresistive elements to maximize sensitivity. As one example simulation, a tensile load of 10 kPa is applied to opposite panels of the bone, normal to the x-axis (σ_{xx}). Symmetry conditions were applied to the interior areas of

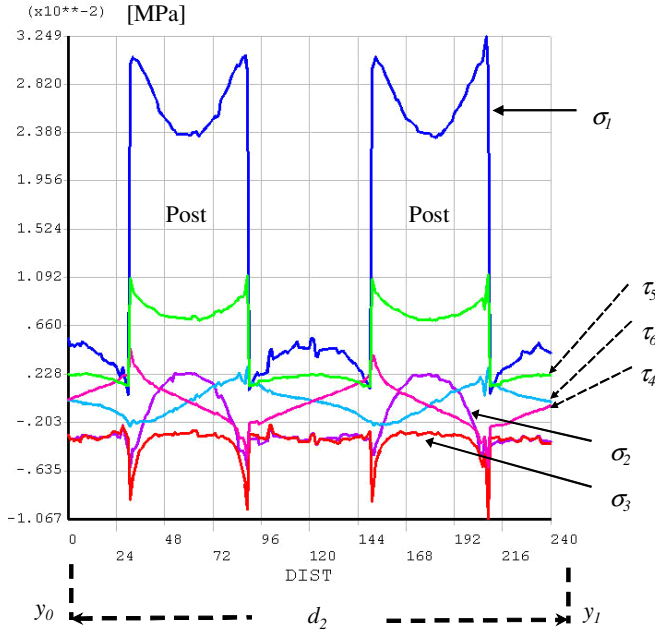


Figure 5. Stress components along sample line d_2 in figure 4 due to 10 kPa tensile stress applied along the x -axis.

the quarter model. Four keypoints were selected to set displacements equal to zero at anchor points. For a tensile load applied in the x -direction, the following keypoints (KP) were defined as shown in figure 4(b): KP-1 located on the yz plane has a displacement $u_z = 0$; KP-2 in the xz plane was set to displacement $u_x = 0$; KP-3 and KP-4 in the xy plane was set to displacement $u_y = 0$. Figure 5 shows the resulting stress components across the bone, posts and beam. The σ_1 component shows a higher stress at the surface of the posts with two peaks near the sides of the post, but lower values within the beam that spans the two posts. This provides insight that the piezoresistive elements should be placed on the posts, and not in the beams, to achieve a higher sensitivity. The other normal stress components (σ_2, σ_3) and shear stress components along the 1, 2 and 3 planes (τ_4, τ_5 and τ_6 , respectively) are much smaller than the σ_1 component. Similar simulations were performed applying tensile stress along the y - and z -axes (σ_{yy}, σ_{zz}), and shear stresses ($\tau_{yz}, \tau_{zx}, \tau_{xy}$) on the side panels of the bone.

2.1.2. Piezoresistive stress detection. The piezoresistance change for a two terminal piezoresistor is

$$\frac{\Delta R}{R} = \pi'_{11}\sigma_1 + \pi'_{12}\sigma_2 + \pi'_{13}\sigma_3 + \pi'_{14}\tau_4 + \pi'_{15}\tau_5 + \pi'_{16}\tau_6, \quad (1)$$

where π'_{ij} are the piezoresistive coefficients, which are dependent on crystal orientation. FEA provides the tensile or shear stress values to calculate (1). The [100] direction for n-type piezoresistors and [110] direction for p-type are chosen since these orientations provide the maximum stress sensitivity due to piezoresistive coefficients being larger in these directions.

The piezoresistance change also depends on the location of the piezoresistors with respect to the die and posts. This

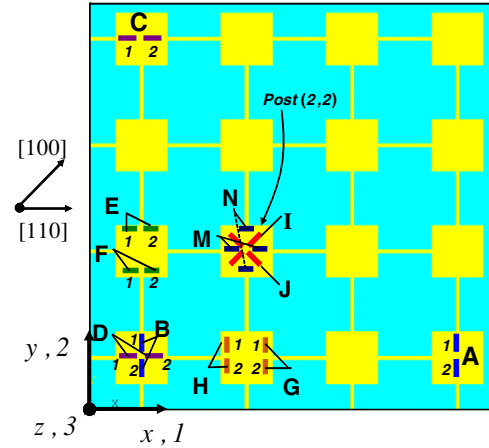


Figure 6. One-quarter layout plan of the 8×8 Si post array, indicating specific orientation in the [110] and [100] direction of the piezoresistors embedded in the posts. All [110] resistors are p-type, except {B, D}, which are n-type. All [100] resistors are n-type.

information is used to build a system of equations to extract the six stress components of interest. The solution determines the six bridge configurations located in six posts to extract the full stress components. Pairs of piezoresistors are placed in the posts in the 12 unique locations $L = \{A, B, C, D, E, F, G, H, M, J, I, N\}$ depicted in figure 6. The figure shows one quarter of the full array. The other quadrants have mirror symmetry.

The fractional resistance change for piezoresistors in the [110] orientation is

$$\begin{aligned} \frac{\Delta R_x}{R_x} &= \frac{1}{2}(\pi_{11}^p + \pi_{12}^p - \pi_{44}^p)\sigma_1 \\ &+ \frac{1}{2}(\pi_{11}^p + \pi_{12}^p + \pi_{44}^p)\sigma_2 + \pi_{12}^p\sigma_3 \end{aligned} \quad (2)$$

$$\begin{aligned} \frac{\Delta R_y}{R_y} &= \frac{1}{2}(\pi_{11}^p + \pi_{12}^p + \pi_{44}^p)\sigma_1 \\ &+ \frac{1}{2}(\pi_{11}^p + \pi_{12}^p - \pi_{44}^p)\sigma_2 + \pi_{12}^p\sigma_3 \end{aligned} \quad (3)$$

$$\begin{aligned} \frac{\Delta R_B}{R_B} &= \frac{1}{2}(\pi_{11}^n + \pi_{12}^n + \pi_{44}^n)\sigma_1 \\ &+ \frac{1}{2}(\pi_{11}^n + \pi_{12}^n - \pi_{44}^n)\sigma_2 + \pi_{12}^n\sigma_3 \end{aligned} \quad (4)$$

$$\begin{aligned} \frac{\Delta R_D}{R_D} &= \frac{1}{2}(\pi_{11}^n + \pi_{12}^n - \pi_{44}^n)\sigma_1 \\ &+ \frac{1}{2}(\pi_{11}^n + \pi_{12}^n + \pi_{44}^n)\sigma_2 + \pi_{12}^n\sigma_3 \end{aligned} \quad (5)$$

for $x = \{C, E, F, M, N\}$ and $y = \{A, G, H\}$ as shown in figure 6. The corresponding equations for the [100] orientation are

$$\begin{aligned} \frac{\Delta R_I}{R_I} &= \frac{1}{2}(\pi_{11}^n + \pi_{12}^n)\sigma_1 \\ &+ \frac{1}{2}(\pi_{11}^n + \pi_{12}^n)\sigma_2 + \pi_{12}^n\sigma_3 + (\pi_{11}^n - \pi_{12}^n)\tau_6 \end{aligned} \quad (6)$$

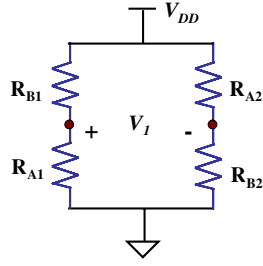


Figure 7. Piezoresistive arrangement for Wheatstone bridge *a*.

$$\frac{\Delta R_J}{R_J} = \frac{1}{2}(\pi_{11}^n + \pi_{12}^n)\sigma_1 + \frac{1}{2}(\pi_{11}^n + \pi_{12}^n)\sigma_2 + \pi_{12}^n\sigma_3 - (\pi_{11}^n - \pi_{12}^n)\tau_6 \quad (7)$$

Simplifying (1) for a {100} silicon wafer shows that the resistance of a single element is dependent on the mechanical normal stress components σ_1 , σ_2 and σ_3 , and xy shear stress component τ_6 . A single resistor element is not capable of extracting an individual stress component due to the four stress component dependency. However, a rosette configuration based on two orientations and two material doping types allows the extraction of the four stress components (σ_1 , σ_2 , σ_3 and τ_6). The main drawback of the rosette configuration is the dependency on temperature variations. In contrast, a piezoresistive bridge within a single post is only sensitive to the normal stress components σ_1 and σ_2 , since these stresses are uniform in such a small region. This can be demonstrated with (2)–(7) for either doping of piezoresistors.

2.1.3. Stress tensor derivation. The piezoresistors are arranged in a set of six Wheatstone bridge configurations, labeled {*a*, *b*, *c*, *d*, *e*, *f*}, in order to cancel common mode influences, particularly temperature. From the structural analysis in the previous section, it is possible to design piezoresistance elements within a bridge to maximize a single component of the stress sensor based on doping type, orientation, location and geometry. As an example, the bridge *a* arrangement is indicated by figure 7, using the four resistors from locations *A* and *B*. Similar arrangements for the other bridges are made with the mappings: *b* from {*C*, *D*}, *c* from {*M*, *N*}, *d* from {*E*, *F*}, *e* from {*G*, *H*} and *f* from {*I*, *J*}.

The magnitude of the internal stress components will be affected not only by the geometry of the transducer, but also with the location *L* on the silicon chip. For instance, regions close to the edges of the chip present a higher stress coupling than center regions. The stress components σ_i and τ_j within the silicon chip are related to the external loads applied to the bone σ_{mn} , where $\sigma_{mn} = [\sigma_{xx}, \sigma_{yy}, \sigma_{zz}, \tau_{yz}, \tau_{xz}, \tau_{xy}]$ by

$$\begin{aligned} \sigma_i &= \sum_m \sum_n L_i^{mn} \sigma_{mn}; & i &= 1, 2, 3 \\ \tau_j &= \sum_m \sum_n L_j^{mn} \sigma_{mn}; & j &= 4, 5, 6, \end{aligned} \quad (8)$$

where L_i^{mn} represents a scaling factor coefficient of *i* with respect to *mn* that depends on the location *L* where the stress component is extracted from the silicon chip.

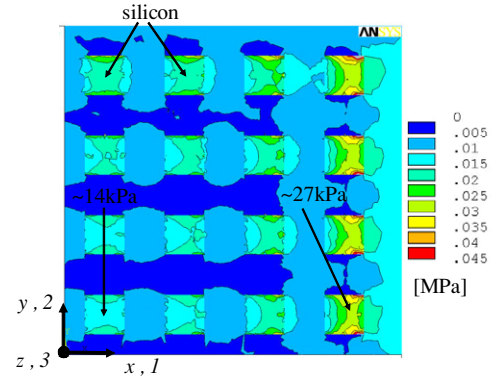


Figure 8. Contour plot of σ_1 stress component due to 10 kPa tensile load on the *x*-axis. The cross section is taken at the top of the silicon in the post.

Figure 8 shows simulation results for a 10 kPa tensile load σ_{xx} applied on the surface of the bone volume. The contour plot of the σ_1 stress component on the surface of the silicon chip illustrates the stress coupling to the external load. A maximum stress of 26 kPa results at the posts near the edge of the chip, whereas the stress is 14 kPa at posts in the middle region of the chip. Similar plots were created for the different internal stress components, for each individual external load applied on the bone. The collected simulation data were used to extract the different scaling factor coefficients L_i^{mn} for the silicon chip.

The piezoresistance change as a function of external loads is determined by substituting (8) into (2). For the bridge *a* with p-type piezoresistors oriented in the [1 1 0] direction in locations (*A*, *B*), the output voltage is

$$V_a = 1/4\{(\Delta R_{A1}/R_{A1} + \Delta R_{A2}/R_{A2}) - (\Delta R_{B1}/R_{B1} + \Delta R_{B2}/R_{B2})\}V_s \quad (9)$$

Similar equations can be derived for the other bridges. A numeric solution to the voltage outputs in the form of $[V] = [K] \cdot [\sigma]$, shown in (10), was obtained by substituting the piezoresistive coefficients and the full set of scaling factor coefficients. In (10), $[V]$ is in units of μV and $[\sigma]$ is in kPa. As desired in the design, bridge *a* has the highest sensitivity to σ_{xx} , bridge *b* has highest sensitivity to σ_{yy} and so on for all six bridges. By inverting $[K]$, it is possible to extract the full stress components from measurements of the six bridge configurations located in the six posts. However, bridge *a* has large cross-axis coupling (more than 14% relative to σ_{xx}) to σ_{yy} , σ_{zz} and τ_{xz} ; bridge *b* has large coupling to σ_{xx} , σ_{zz} and τ_{yz} ; and bridge *c* has large coupling to σ_{xx} and σ_{yy} . The bridges *d*, *e* and *f* have small cross-axis coupling. The condition number for $[K]$ is 6.86, which is relatively large and translates into an error sensitivity for stress extraction using $[K]^{-1}$ of no worse than 7% of the error in the measured bridge

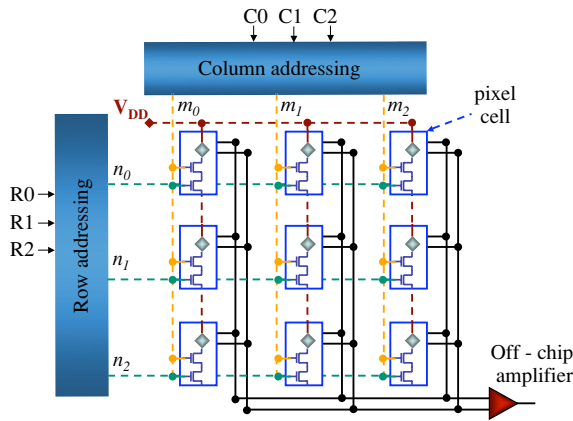


Figure 9. Basic CMOS array architecture.

voltages due to a 1% error in the input.

$$\begin{bmatrix} V_a \\ V_b \\ V_c \\ V_d \\ V_e \\ V_f \end{bmatrix} = \begin{bmatrix} -0.807 & 0.217 & -0.274 & 0.081 & -0.299 & 0.005 \\ 0.217 & -0.807 & -0.262 & -0.299 & 0.081 & 0.004 \\ -0.064 & -0.136 & 0.290 & -0.011 & 0.029 & -0.011 \\ 0.049 & -0.148 & 0.058 & -1.144 & -0.011 & -0.052 \\ -0.148 & 0.049 & 0.062 & -0.011 & -1.144 & -0.017 \\ -0.016 & -0.016 & 0.026 & 0.024 & 0.024 & 1.938 \end{bmatrix} \cdot \begin{bmatrix} \sigma_{xx} \\ \sigma_{yy} \\ \sigma_{zz} \\ \tau_{yz} \\ \tau_{xz} \\ \tau_{xy} \end{bmatrix} \quad (10)$$

3. Circuit design and implementation

3.1. Topology

The topology of the circuit system for the bone stress sensor array is based on the basic row and column select components in a CMOS imager. Since the entire chip consists of an array of posts, the bridge circuits must be distributed within the posts to take advantage of the available silicon area. The transducer array requires low power consumption and it must have the ability to access the various bridges in the array. Figure 9 shows a simplified schematic of the CMOS array sensor architecture realized with the use of row/column decoders to access each pixel from the array and transfer the sensed voltage to external electronics. The piezoresistive bridges are shown as small diamonds in the figure. By selecting power to each bridge only when being read out, the overall power consumption for the system is reduced. The detailed schematic of the pixel cell implemented for the array sensor is shown in figure 10.

The pixel consists of the piezoresistor bridge circuit with its outputs routed to two selector transistors, M_1 and M_2 . Both output signals are routed directly to bondpads, which are connected to an off-chip amplifier. The signals from

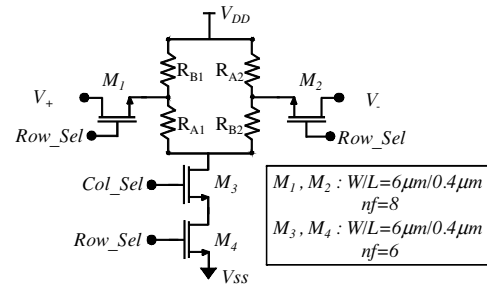


Figure 10. Pixel cell schematic for a sensor array.

the multiplexer control logic are column select, Col_sel , and row select, Row_sel . The chip supply voltage is $V_{DD} = 3.3$ V. Transistors M_3 and M_4 switch power to the cell when a particular row and column is selected. The nominal resistance value of each bridge is 6 k Ω .

3.2. Layout

The 8×8 sensor array layout shown in figure 11(a) was designed in the Jazz Semiconductor 0.35 μm BiCMOS process. The chip size is 1.6 mm by 1.25 mm. Bondpads for wired operation are located at the periphery of the array. The silicon area surrounding the array eliminates the possibility of experimentally validating the piezoresistive bridges a and b , which require piezoresistors located at the chip periphery as indicated in figure 6. However, the prototype sensor array design is based on the same theory described in section 2 and allows validation of the other bridge designs. In all, six types of piezoresistive bridges were implemented with the resistor orientations and doping shown in figure 11(b). The ‘bridge I’ arrangement is located in a single post with four p-type [1 1 0] resistors where two are oriented along the 1 (x) axis and the other two are oriented along the 2 (y) axis. Bridge II is similar to bridge I, but with n-type resistors oriented along the 2 (y) axis. Bridge III is also similar to bridge I, but uses all n-type resistors. The remaining bridges IV, V and VI, correspond to the post layout in bridges c , d and e , respectively, from section 2. Bridge f was not implemented. The piezoresistors were 11.75 μm long and 2 μm wide giving nominal resistances of $R_n = 6.4$ k Ω and $R_p = 0.7$ k Ω for n-type and p-type doping, respectively. The custom-made p-type resistor size was unintentionally set to this relatively low resistance value. The six bridge types were replicated eight times within the 8×8 array, and four additional bridge types were replicated four times.

Decoders for column and row addressing occupy a small area (250 $\mu\text{m} \times 30 \mu\text{m}$) next to the I/O bondpads. The posts are 60 $\mu\text{m} \times 60 \mu\text{m}$ in area, which is large enough to contain the bridge circuits and row selector switches. The beams, which span from post-to-post, are 60 μm long \times 5 μm wide. Vertical-oriented beams carry the V_+ , V_- and Col_sel signals, whereas horizontal-oriented beams are used to route V_{DD} and Row_sel signals. The top metal is connected to ground. This routing is possible because of the four metal layers available in the CMOS process.

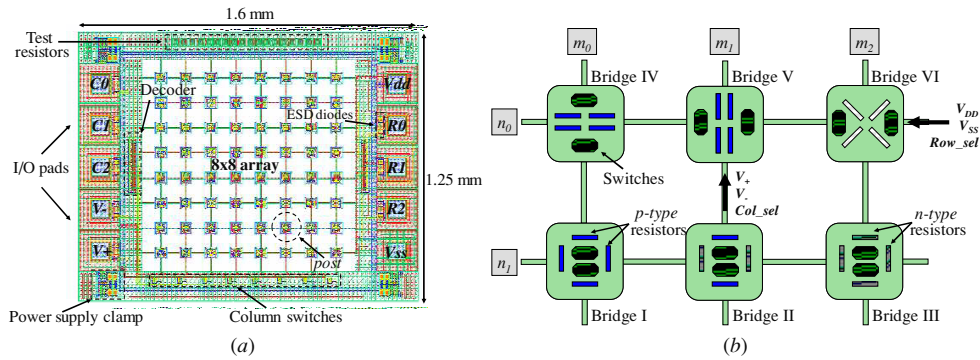


Figure 11. Layout view of the 8 × 8 array bone stress sensor. (a) Full layout of the 1.6 mm × 1.25 mm sensor chip. (b) Layout detail of sensor elements.

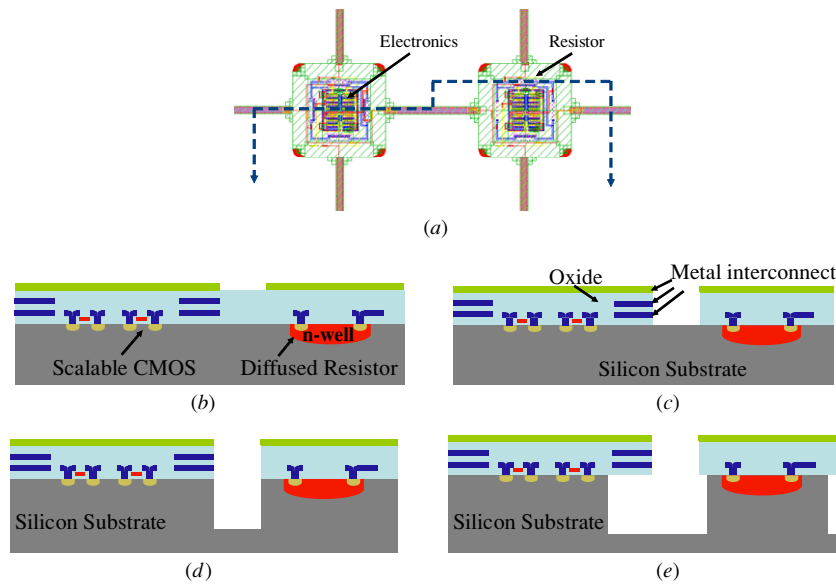


Figure 12. Layout view and cross section of the post-CMOS process. (a) Layout view of two posts. (b) CMOS chip from foundry. (c) Oxide etch. (d) DRIE. (e) Isotropic etch.

4. Prototype device fabrication

4.1. MEMS post-CMOS processing

After completion of the foundry CMOS processing, a MEMS process was used for the microfabrication of the sensor posts. The process is based on prior work in our group to fabricate microstructures with high-aspect-ratio (about 5:1) composite-beam suspensions by using conventional CMOS processing followed by a sequence of maskless dry-etching steps [23, 24]. Figure 12 summarizes the post-CMOS MEMS fabrication steps. The CMOS chip received from the foundry consists of a silicon substrate with a thickness of approximately 350 μm. The first step is an oxide reactive-ion etch (RIE) with a PlasmaTherm 790 system. The oxide etch time is approximately 5 h to etch through the 9 μm thick dielectric stack. The gases used are CHF₃ (22.5 sccm) and O₂ (16 sccm), with a pressure of 100 mT and a power setting of 100 W. Once the silicon substrate is exposed, the chip is transferred to a Surface Technology System inductively coupled plasma reactor to

perform a timed deep Si RIE step to a trench depth of 60 μm. The final process step is a short Si isotropic etch to undercut and release the 5 μm wide beams.

Electronics in the posts were placed at least 10 μm from the Si trench edge to prevent failure of circuits because of Si micromachined undercut. Figure 13 shows SEMs of the released sensor array chip. The total etch depth is 60 μm, and the undercut of the posts is approximately 3 μm. This undercut was not included in the stress simulation of the 60 μm × 60 μm posts due to meshing limitations of our ANSYS license. The undercut might increase the stress value estimation as it is shown in section 5.

4.2. Embedding device in tensile testing specimen

Mechanical characterization of the sensor array, as described in the following section, was performed by first mounting it to a custom printed circuit board (PCB), to provide access to external wiring, embedding the array/PCB in a ‘dog-bone’ ASTM standard test specimen (shown in figure 14(a)), and then subjecting the completed test specimen

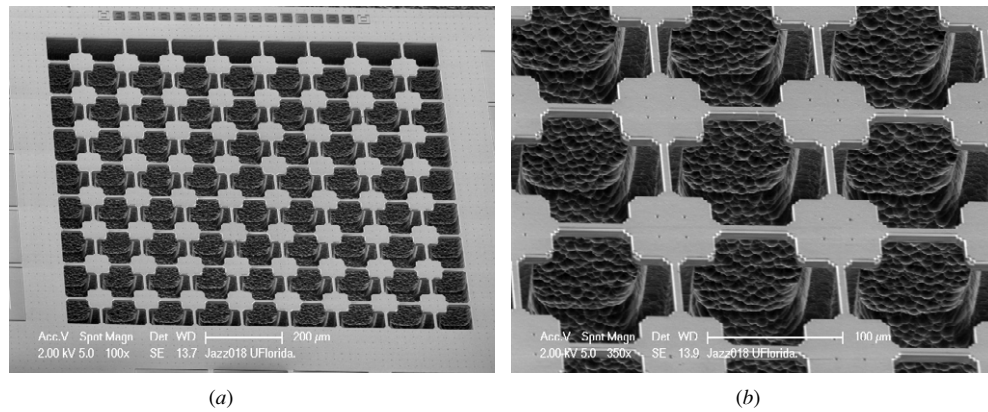


Figure 13. SEMs of the bone stress sensor after micromachining the 0.35 μm BiCMOS chip. (a) Released 8 \times 8 sensor array. (b) Detail of posts with rounded corners.

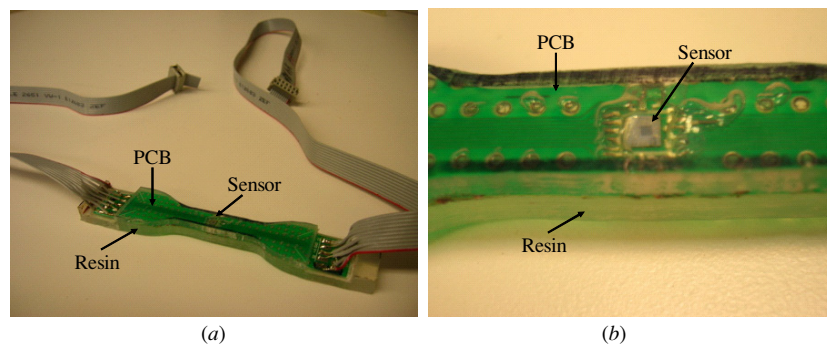


Figure 14. ASTM D 638 specimen with embedded chip.

to controlled stresses. The PCB was thinned down to 300 μm to decrease its stiffness and minimize its overall effect on the specimen's mechanical properties. A Batwing 22 lead frame from standard Surface Mount Technology packages [25] was bonded to the PCB, and then the CMOS chip was bonded to the lead frame using a silver conductive epoxy based adhesive (CW2400 CircuitWorks[®], ITW Chemtronics[®]). Connections from the chip pads were then wire bonded to the lead frame as shown in figure 14(b).

The material for the dog-bone specimen was Veriflex[®] resin [26], which has a compressive modulus of 1.465 GPa, similar to cancellous bone, and which also has temperature-dependent elastic properties to be able to simulate different bone stiffnesses. The resin solution was first mixed and placed in a vacuum desiccator to remove air bubbles. The solution was then poured to a thickness of 0.12" into a 3" \times 5" rectangular mold made with glass sheets. The sample was cured in an oven at 75 $^{\circ}\text{C}$ for 36 h. The PCB was then bonded to this resin sheet using an epoxy-based adhesive (#4001, extra-fast setting epoxy, Hardman). More resin was then poured over and cured on the top of the first sheet to enclose the chip. After curing and release, the two layer resin structure was cut into a dog-bone test specimen according to ASTM D638 [27].

Possible mechanical failure modes of the sensor most likely will occur at the 9.63 μm wide by 5.3 μm tall by 60 μm long CMOS-MEMS suspended beams interconnecting

the silicon posts rather than within the silicon posts, which are much larger. Failure from stress could originate from axial stress or by in-plane shear stress. However, no failure was observed in any of the embedded tests that were performed. Furthermore, a destructive test was performed to verify the mechanical properties of the resin and no fracture or delamination was observed in the sensor. In this test, a specimen was subject to a tensile load in a MTS Bionix 858 load test system at a rate of 2 mm in 2 min. The maximum load at failure was 1.2 kN.

The oxide-metal beams that span from post to post are estimated to have a fracture strain greater than 1%, corresponding to a normal stress of greater than 600 kPa and larger than the intended applied loads. We believe the 1% strain estimate is conservative, since the axial stress fracture limit of silicon dioxide fibers is listed as 8.4 GPa [28].

In the case of shear failure, for a typical stress of 10 kPa applied to the arm the corresponding shear stress on the Si posts is only 0.8 kPa, and 4–5 kPa at the beams and posts corners. The shear fracture stress of 53 μm thick oxide microstructure ring membranes has been measured at 3–5 MPa [29]. The strength of a given structure depends greatly on the shape and presence of any defects, especially sharp corners. The current design of the bone stress sensor includes round corners at Si posts and chamfered intersections at the end of suspended beams for stress relief.

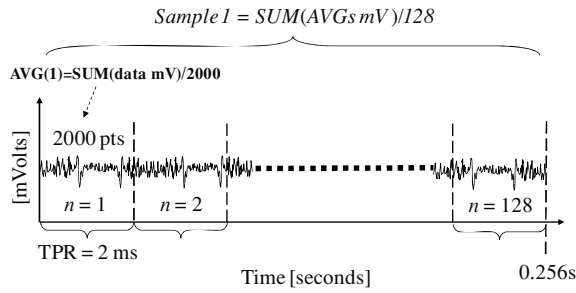


Figure 15. Oscilloscope configuration for LabView data capture.

5. Experimental results

5.1. Tensile testing

A custom-made tensile test rig was built consisting of a fixed gripper clamped to the top part of the dog-bone specimen and a free clamp at the other end where calibrated weights were applied (100–500 gm). Data were recorded with National Instruments (NI) LabVIEW software. A NI-USB-6009 data acquisition unit was connected through the computer USB port. Six data lines (bits) were used to activate the row decoder (3 bits) and the column decoder (3 bits), in order to access the 8×8 sensor array. The sensor's differential output was connected to an off-chip precision instrumentation amplifier (Analog Devices AD624) with a voltage gain of 200. The AD624 is a high precision, low noise ($0.2 \mu\text{Vpp}$, 0.1 to 10 Hz) instrumentation amplifier designed primarily for use with low level transducers. The AD624C has an input offset voltage drift of less than $0.25 \mu\text{V } ^\circ\text{C}^{-1}$, output offset voltage drift of less than $10 \mu\text{V } ^\circ\text{C}^{-1}$, CMRR above 80 dB at unity gain (130 dB at $G = 500$), and a maximum nonlinearity of 0.001% at $G = 1$. A NI GPIB USB-B controller sampled data from an Agilent 54622A oscilloscope by averaging 2000 data points in a 2 ms time per record (TPR) as shown in figure 15. A total of 128 records were collected and later averaged in software. The corresponding total averaging time for one measured sample with this configuration was 256 ms ($2 \text{ ms} \times 128 \text{ records}$).

Figure 16 shows the output of several type III bridges located at the sixth column of the 8×8 array bone stress sensor prototype. This type of bridge is sensitive to tensile or compressive stress. The total averaging time for five samples was 1.28 s for all data. The measured standard deviation for this data set at the output of the off-chip amplifier was $226 \mu\text{V}$. Assuming a 10 dB SNR, the minimum detectable signal within the mock bone/PCB assembly is 23.8 kPa (2.38 N). This value is much higher than the desired resolution since most of the load is transferred to the PCB since, although the PCB is thin, it is made of a much stiffer material than the mock bone and thus shunts a significant amount of stress.

The initial measurements demonstrate the basic functionality of the stress sensor to detect normal stress. However, to better characterize the device it will be necessary to avoid the hardwired test approach requiring a PCB. This issue will be addressed in the next version of sensor design by using an on-chip wireless system. In addition, an on-chip amplifier would increase the output signal and reduce some

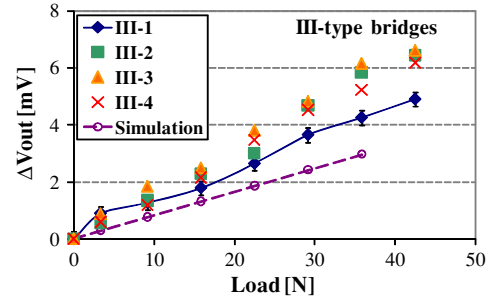


Figure 16. Output for type III bridges in tension.

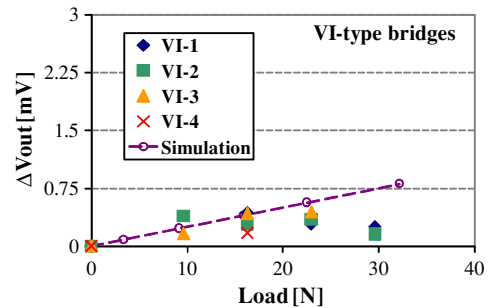


Figure 17. Output for type VI bridges in tension.

of the noise originated by the wiring from the PCB to the testing instruments. Also, without the PCB, the test specimen preparation will be simplified, and reduce the bubble formation due to air trapped between the PCB and the first resin layer. A reference gage could also be attached during the test specimen preparation to verify the axial loads during tensile or bending tests.

The applied test loads correspond to a stress range from 30 kPa to 400 kPa. The stress sensitivity prior to amplification is $190 \mu\text{V V}^{-1} \text{MPa}^{-1}$. The output change follows the trend of the simulation data shown in figure 16. The nonlinearity in the bridge's voltage output is believed to be due to non-uniformity in the resin around the device. Figure 17 shows the output of several type IV bridges located at the sixth column of the 8×8 sensor array. These pixels are sensitive to shear stress. While these sensor bridges have highly nonlinear output with tensile load, their measured sensitivity to axial stress is small, as desired. Further experimental assessment of this bridge design to validate its utility in shear stress detection is needed.

5.2. Bend testing

A four-point bending test rig was built to measure the behavior of the sensor under compressive and tensile loads. Figure 18 shows a schematic of the bending test rig, which is based on a G22G flexure fixture. Two forces act on the upper side of the specimen, with a span of $L/3$, where L refers to the major span between the bottom supports. Figure 19 shows the cross section of a simply supported loaded beam, with a magnified bending caused by the load. The applied load to the beam and the support force generate internal shearing forces and internal torque called bending moments. For clarity, the

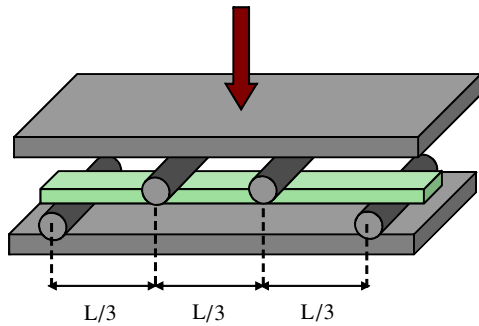


Figure 18. Schematic and model of a 4-point bend test fixture.

second diagram does not show vertical shear force, but shows horizontal forces ($-F_x$ and $+F_x$). As the beam bends, the top region of the beam is put into compression and the bottom region of the beam is put into tension. This results in internal axial forces (horizontal, x -axis) acting in the beam. The chip is located approximately 1.5 mm with respect to the axial centerline of the beam.

Figure 20 shows the output of replicate [1 1 0] n-type bridges located in column 2 during bending in tension, whereas figure 21 shows the output during bending in compression. When the specimen (figure 14) is placed in the test fixture (figure 18) in the normal orientation, the sensor is above the axial centerline of the beam. In this case, the top region is put into compression. During tension, the test specimen is flipped upside down, and the sensor experiences a tensile force. The observed standard deviation for this data set at the output of the off-chip amplifier was $160 \mu\text{V}$. For a 10 dB SNR, the minimum detectable signal is 18 kPa.

All of the 64 bridges were tested under bending stress and all were functional. As expected from the analysis in section 2, the bridges closer to the edge have a higher output.

5.3. Temperature characterization

The bridge circuit eliminates common-mode changes in the outputs of the stress sensors due to temperature variations and drift. However, the rest of the electronics, including the switches to power each pixel, the decoders and the electrostatic discharge protection were not designed to be immune to temperature changes. A circuit simulation was performed to quantify bridge current as a function of temperature, and

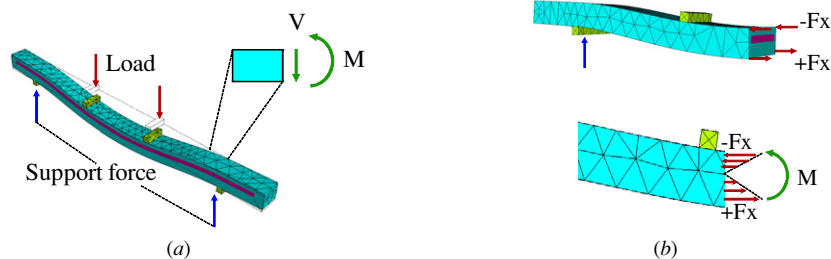


Figure 19. Resultant forces and moments due to beam bending. (a) Beam section showing shear force and bending moment. (b) Axial forces due to beam bending.

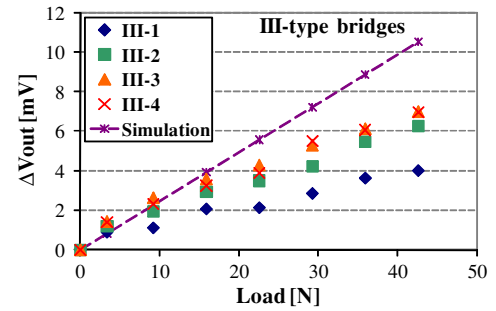


Figure 20. Output for type III bridges during bending in tension.

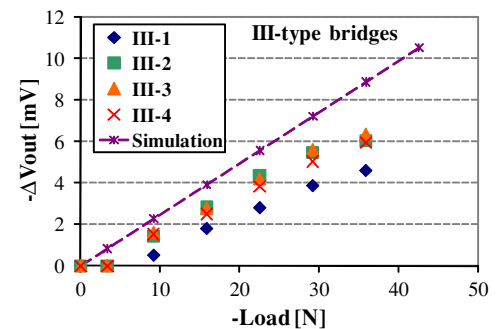


Figure 21. Output for type III bridges during bending in compression.

the results were compared to experimental data. A released chip was wirebonded to a metal lead frame on a thinned PCB. The sensor and PCB were placed inside an oven to record the bridge current, I , across a temperature range from $20 \text{ }^\circ\text{C}$ to $75 \text{ }^\circ\text{C}$, with data for two bridges shown in figure 22. The temperature sensitivity of the measured current matches that obtained through simulation. The offset in the plot is due to the difference between the nominal and actual value R_0 for the designed resistors. The simulation uses $6.4 \text{ k}\Omega$ resistors and the actual resistor values were within 7% of the designed value. There is also an offset between the [1 1 0] and the [1 0 0] resistors, since the latter were made with custom layout by rotating the resistors by 45° using a Manhattan stairstep approximation. The power consumed by each bridge during a measurement cycle is a maximum of $775 \mu\text{W}$ (3.3 V supply). The total energy expended for sequential activation of six bridges is 1.2 mJ. The power could be lowered by lowering the supply voltage. Larger values of piezoresistors would also

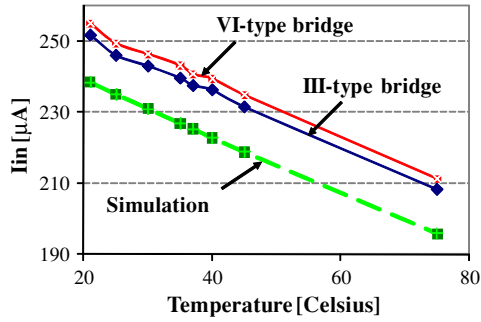


Figure 22. Current I_{in} for two III-type and VI-type bridges as a function of temperature.

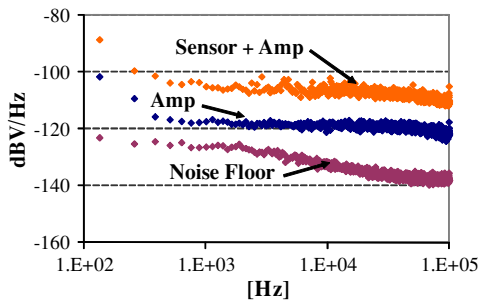


Figure 23. Measured output referred noise.

lower power, however their size is constrained by the available silicon post area. Average power would be greatly reduced by running the sensor at a low duty cycle, for example once every few seconds. In wireless power operation, a capacitor to store the scavenged energy would be required to drive the bridge at its duty cycle.

5.4. Noise analysis

The piezoresistors forming the stress sensors, have inherent noise voltage

$$\sqrt{\bar{v}_{n,res}^2} = \sqrt{4k_B T R \Delta f} \quad (11)$$

where T is the temperature in Kelvin, k_B is Boltzmann's constant $1.38 \times 10^{-23} \text{ m}^2 \text{ kg s}^{-2} \text{ K}^{-1}$, R is the resistance and Δf is the circuit bandwidth in Hz. A 6455Ω resistive bridge in a 1 Hz bandwidth will add noise of $10.3 \text{ nV Hz}^{-1/2}$. The off-chip amplifier has an input referred noise of $4 \text{ nV Hz}^{-1/2}$. Adding the noise power together yields a total theoretical noise level of $11.1 \text{ nV Hz}^{-1/2}$. The measured output referred noise of the amplifier and of the total sensor/amplifier system is shown in figure 23. The total measured input referred noise was $17.6 \text{ nV Hz}^{-1/2}$, which was well above the spectrum analyzer noise floor and close to the calculated value. For a minimum in-plane shear stress of 100 Pa, the expected output voltage from the bridge is $0.2 \mu\text{V}$. Using the $17.6 \text{ nV Hz}^{-1/2}$ noise voltage in the 256 ms averaging time the respective SNR is 15.2 dB. Thus, the intrinsic noise of the sensor is sufficient for the bone stress monitoring application.

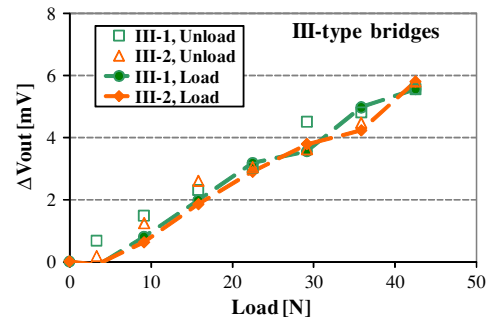


Figure 24. Hysteresis behavior in a four-point bending fixture for III-type bridges.

5.5. Hysteresis

Hysteresis behavior was assessed using the bending test rig described above. Figure 24 shows the output voltage change during loading (dashed lines) and unloading (opened markers) during bending. The overall characteristic of the sensor shows good linearity during loading and unloading for all the pixels tested. The mean relative difference between the two sets of values is lower than 10% of the full scale. These voltage differences are attributed to movement in the fixture and/or error due to noise during the measurement. No noticeable hysteresis was observed during different tests.

6. Conclusions

The results presented in this paper are a first step in the development of an implantable wireless piezoresistive bone stress sensor with active electronics readout. Texturing of the silicon CMOS chip surface into $60 \mu\text{m} \times 60 \mu\text{m} \times 60 \mu\text{m}$ tall posts will help to enhance cell growth and osteointegration. An initial wired prototype of the multi-axis transducer with an 8×8 array of silicon posts with CMOS electronics was able to successfully measure compressive and tensile stresses. The experimental prototype provides a partial validation of the concept in section 2. The measured input referred noise of $17.6 \text{ nV Hz}^{-1/2}$ is sufficient for the bone stress application, however a wireless chip prototype without rigid PCB wiring is required to detect the targeted 100 Pa stress levels. Future designs can modulate the bridge current to reduce the flicker noise.

The on-chip CMOS electronics enables the measurement of internal normal and shear stress data for all three axes. A general theoretical formulation was derived for the use of piezoresistive bridges within the sensor's surface topography. By incorporating an array of six Wheatstone bridges based on the selection of p-type and n-type piezoresistive elements relative to the silicon crystallographic orientation, it is possible to determine the normal and shear stresses under a single load in a bone-like material. In order to resolve all the stress elements, piezoresistors in at least two of the bridges must be placed far apart on the chip, as determined through simulation. In the future, piezoresistors located in posts at the periphery of the chip will enable full validation of the array concept in section 2 through experimental measurement and extraction of

all six normal and shear stress components for a given external load. Finally, the condition number of the matrix $[K]$ in (10) could be decreased with sensor design optimization to increase axial sensitivity and reduce cross-coupling. Parameters such as piezoresistive location, shape of silicon posts or incorporation of polysilicon piezoresistors on beams can be used to improve the current design.

Design of an on-chip coil, power conditioning electronics and RF communication electronics on the CMOS chip is challenging, but feasible in future work. Implantation depths over which RF telemetry will have to be established will depend on the specific location where the sensor will be implanted and on the physical characteristics of the patient. Interpretation of the measured signal will require knowing the orientation of the sensor within bone. Adjusting the orientation of the external coil to maximize RF coupling should provide the required information, however this represents another system design challenge.

The bone stress sensor may, in the long-term, enable *in vivo* experiments for a deeper understanding of bone tissue structure and function. Its capability to measure and quantify biomechanical properties *in vivo* would potentially make it an enabling technology for many applications, including as a tool to gain new knowledge about bone regeneration and remodeling at the micro-scale and aid in the development and verification of new graft materials, and, ultimately to provide improved information in real-time for clinical management of osteogenic diseases and trauma.

Acknowledgment

This work was supported in part by The Pennsylvania Infrastructure Technology Alliance and The Technology Collaborative (former Pittsburgh Digital Greenhouse). The authors would also like to thank the members of the Carnegie Mellon Nanofabrication Facility for assistance with fabrication, and Duquesne University for assistance with cell experiments.

References

- [1] Gilsanz V 1998 Bone density in children: a review of the available techniques and indications *Eur. J. Radiol.* **26** 177–82
- [2] Baroncelli G I 2008 Quantitative ultrasound methods to assess bone mineral status in children: technical characteristics, performance, and clinical application *Pediatr. Res.* **63** 220–8
- [3] Hans D and Krieg M-A 2008 The clinical use of quantitative ultrasound (QUS) in the detection and management of osteoporosis *IEEE Trans. Ultrason. Ferroelectr. Freq. Control* **55** 1529–38
- [4] Nicholson P H F 2008 Ultrasound and biomechanical competence of bone *IEEE Trans. Ultrason. Ferroelectr. Freq. Control* **55** 1539–45
- [5] Nokes L D M 1999 The use of low-frequency vibration in orthopaedics *Proc. Inst. Mech. Eng.* **213** 271–90
- [6] Bergmann G, Graichen F, Siraky J, Jendrynski H and Rohlmann 1988 A Multichannel strain gauge telemetry for orthopaedic implants *J. Biomech.* **21** 169–76
- [7] Burny F et al 2000 Concept, design and fabrication of smart orthopedic implants *Med. Eng. Phys.* **22** 469–79
- [8] Elvin N, Elvin A and Spector M 2000 Implantable bone strain telemetry sensing system and method *US Patent* 6,034,296
- [9] Webster D J, Morley P L, Lenthe G H V and Muller R 2008 A novel *in vivo* mouse model for mechanically stimulated bone adaptation—a combined experimental and computational validation study *Comput. Methods Biomech. Biomed. Eng.* **11** 435–41
- [10] Hsieh M C, Fang Y K, Ju M S, Chen G S, Ho J J, Yang C, Wu P M, Wu G and Chen T Y F 2001 A contact-type piezoresistive micro-shear stress sensor for above-knee prosthesis application *J. Microelectromech. Syst.* **10** 121–7
- [11] Hoshaw S J, Fyhrie D P, Takano Y, Burr D B and Milgrom C 1997 A method suitable for *in vivo* measurement of bone strain in humans *J. Biomech.* **30** 521–4
- [12] Tang W 2005 Biomechanics at the micro scale *Emerging Information Technology Conf.* pp 1–5
- [13] Yang G, Bailey V, Wen Y H, Lin G, Tang W and Keyak J 2004 Fabrication and characterization of microscale sensors for bone surface strain measurement *Proc. IEEE Sensors* **3** 1355–8
- [14] Benzel E, Kayanja M, Fleischman A and Roy S 2006 Spine biomechanics: fundamentals and future *Clin. Neurosurg.* **53** 98–105
- [15] An Y H 2000 *Mechanical Testing of Bone and the Bone-Implant Interface* ed Y H An and R A Draughn (Boca Raton, FL: CRC Press) pp 41–64
- [16] Cil A, Veillette C J, Sanchez-Sotelo J, Sperling J W, Schleck C and Cofield R H 2009 Revision of the humeral component for aseptic loosening in arthroplasty of the shoulder *J. Bone Joint Surg. Br.* **91** 75–81
- [17] Melik R, Perkgoz N K, Unal E, Puttlitz C and Demir H V 2008 Bio-implantable passive on-chip RF-MEMS strain sensing resonators for orthopaedic applications *J. Micromech. Microeng.* **18** 1–9
- [18] Alfaro J F, Weiss L E, Campbell P G, Miller M C, Heyward C, Doctor J S and Fedder G K 2005 Bioimplantable bone stress sensor *27th Ann. Int. Conf. of the Engineering in Medicine and Biology Society, IEEE-EMBS* vol 1 pp 518–21
- [19] Chehroudi B, McDonnell D and Brunette D M 1997 The effects of micromachined surfaces on formation of bonelike tissue on subcutaneous implants as assessed by radiography and computer image processing *Biomed. Mater. Res. J.* **34** 279–90
- [20] Albrektsson T and Hansson H A 1986 An ultrastructural characterization of the interface between bone and sputtered titanium or stainless steel surfaces *Biomaterials* **7** 201–5
- [21] Johansson C B, Hansson H A and Albrektsson T 1990 Qualitative interfacial study between bone and tantalum, niobium or commercially pure titanium *Biomaterials* **11** 277–80
- [22] Heyward C 2004 The importance of Si surface topography in the attachment, proliferation, and differentiation of human adult mesenchymal stem cells *Masters Thesis* Duquesne University Pittsburgh, PA
- [23] Fedder G K, Santhanam S, Reed M L, Eagle S C, Guillou D F, Lu M S-C and Carley L R 1997 Laminated high-aspect-ratio microstructures in a conventional CMOS process *Sensors Actuators A* **57** 103–10
- [24] Xie H, Zhu X, Erdmann L, Gabriel K J and Fedder G K 2000 A novel micromachining process for high-aspect-ratio CMOS-MEMS *Tech. Dig. of Solid-State Sensor and Actuator Workshop (Hilton Head Island, SC)* vol 1 pp 77–80
- [25] Co-planar Inc 2006 Precision stamped metal and mylar components, Denville, NJ <http://www.co-planar.com/>
- [26] CRG Industries LLC 2006 Veriflex[®] shape memory polymer resin systems, Cornerstone Research Group, Inc., Dayton, OH <http://www.crgip.net/veriflex.htm>

- [27] American Society for Testing and Materials 2003 ASTM D638-03 Standard test method for tensile properties of plastics, Philadelphia, PA <http://www.astm.org/>
- [28] Petersen K E 1982 Silicon as a micromechanical material *Proc. IEEE* **70** 420–57
- [29] Zhang C and Najafi K Fabrication of thick silicon dioxide layers using DRIE, oxidation and trench refill *Proc. 15th IEEE Int. Conf. on Micro Electro Mechanical Systems (MEMS '02) (Las Vegas, NV, January 20–24 2002)* pp 160–3